PLANT SCIENCES

Photonic paper: Multiscale assembly of reflective cellulose sheets in *Lunaria annua*

G. Guidetti[1,2], H. Sun[3], B. Marelli[3], F. G. Omenetto[1,2,4]*

Bright, iridescent colors observed in nature are often caused by light interference within nanoscale periodic lattices, inspiring numerous strategies for coloration devoid of inorganic pigments. Here, we describe and characterize the septum of the *Lunaria annua* plant that generates large (multicentimeter), freestanding iridescent sheets, with distinctive silvery-white reflective appearance. This originates from the thin-film assembly of cellulose fibers in the cells of the septum that induce thin-film interference–like colors at the microscale, thus accounting for the structure's overall silvery-white reflectance at the macroscale. These cells further assemble into two thin layers, resulting in a mechanically robust, iridescent septum, which is also significantly light due to its high air porosity (>70%) arising from the cells' hollow-core structure. This combination of hierarchical structure comprising mechanical and optical function can inspire technological classes of devices and interfaces based on robust, light, and spectrally responsive natural substrates.

INTRODUCTION

Structural color has captured the fascination of optical researchers through numerous observations throughout history, both in naturally occurring structures and in the animal world (*1*–*3*). Plants have also evolved structural colors to fulfill a variety of functions (*4*–*7*): Structurally colored leaves (*8*–*10*), flowers (*11*, *12*), and fruits (*4*, *5*, *13*, *14*) are used by plants to regulate light harvesting (*8*, *15*–*17*) and attract pollinators (*6*, *7*), while they are also believed to promote seed dispersal (*4*, *5*). The few, so far, described plants whose fruits are structurally colored are understory species living in tropical regions, whose fruits reflect light spanning from deep metallic blue to green when ripe. The brilliant coloration of these small, spherical fruits originates from the interference of light with the periodic assembly of cellulose fibrils, which can form either multilayer stacks as in *Elaeocarpus angustifolius* (*13*) and *Delarbrea michieana* (*14*) or helicoidal architectures as in *Pollia condensata* (*4*) and *Margaritaria nobilis* (*5*, *18*). For some of these species, the fruits' structural coloration is thought to be functional for attracting birds that could promote their seed dispersal (*4*, *5*). The photonic architectures responsible for this structural coloration develop inside the secondary cell wall of the fruits' pericarp, constituting one of the outermost layers of their more complex morphology. Here, we discuss a structurally colored fruit that differentiates from the other few structurally colored fruits documented so far for its larger size, flat shape, temperate growing environment, and spectral selectivity. The *Lunaria annua* Linnaeus temperate plant (*19*) produces a fruit with a photonic structure in the septum, which is large, microscopically flat, freestanding, and silvery-white. It consists of two adhering laminae of cellulose with broadband reflection as a consequence of multiple thin-film interference in the cladding of the hollow fibrillar hierarchies in the cell wall of the cells that form the septum (Fig. 1).

[1]Department of Biomedical Engineering, Tufts University, 4 Colby Street, Medford, MA 02155, USA. [2]Silklab, Tufts University, 200 Boston Avenue, Medford, MA 02155, USA. [3]Department of Civil and Environmental Engineering, Massachusetts Institute of Technology, 77 Massachusetts Ave., Cambridge, MA 02139, USA. [4]Department of Physics, Tufts University, 4 Colby Street, Medford, MA 02155, USA.
*Corresponding author. Email: fiorenzo.omenetto@tufts.edu

RESULTS

L. annua seedpod

L. annua Linnaeus is a biennial dicot herbaceous weed that belongs to the family of Brassicaceae, and it originates from southeastern Europe (*20*–*22*). *Lunaria* grows in semishady environments, and it produces green flat nonfleshy fruits (*23*, *24*), the seedpods, which reveal a silvery septum in their interior when ripe (Fig. 1, A and B). The *Lunaria* seedpods consist of a dehiscent capsule of three flat elliptical membranes, as typical of the genus *Lunaria* (*25*, *26*): the two external matte valves create a silicle for the development of the seeds, which originate from the internal silvery-white partitioning false septum (Fig. 1A). In the *Lunaria* genus, the fruit shape is believed to have been optimized by the plant to promote anemochorous seed dispersal, hence the light, large, and flat elliptical shape of the valves and, possibly incidentally, of the septum (*22*, *24*, *26*). During growth, the seeds attach to the valves so that when the mature fruit opens due to the accumulated tension in the valves, the valves detach from the replum and disperse the glued seeds via anemochory (*26*–*28*). On the contrary, the septum remains on the plant, displaying a notably shiny appearance that justifies *Lunaria*'s popular use as ornamental plant. Contrary to the septum, the *Lunaria* seeds have been long studied for their tissue morphology (*29*, *30*), as a source of nervonic acid (*31*), lunarine (*32*), and oil (*33*).

L. annua septum morphology

The *L. annua* septum is elliptical (3.1 ± 0.4 cm × 4.6 ± 0.4 cm, ± SD; N = 22, N = number of independent measurements) and is composed of cellulose. X-ray diffraction (XRD) characterization of the *Lunaria* septum showed peaks at 2θ ~14° to 17°, ~22°, and 34° (fig. S1), which correspond, respectively, to the {100}, {200}, and {400} planar orientations of the crystalline structure of cellulose I, which is the naturally occurring crystalline form of cellulose (*34*). The septum is found to be highly reflective on both sides, with its white and brilliant appearance reminiscent of the structural color observed in nacre (*35*). The septum macroscopic texture is homogenous (Fig. 1B), except for the funicles, which bring nutrients to the seeds. Upon closer inspection, thin-film interference–like colors spanning the visible range can be observed (Fig. 1C). To elucidate the origin of this optical behavior, we carried out structural analysis of the septum. Scanning

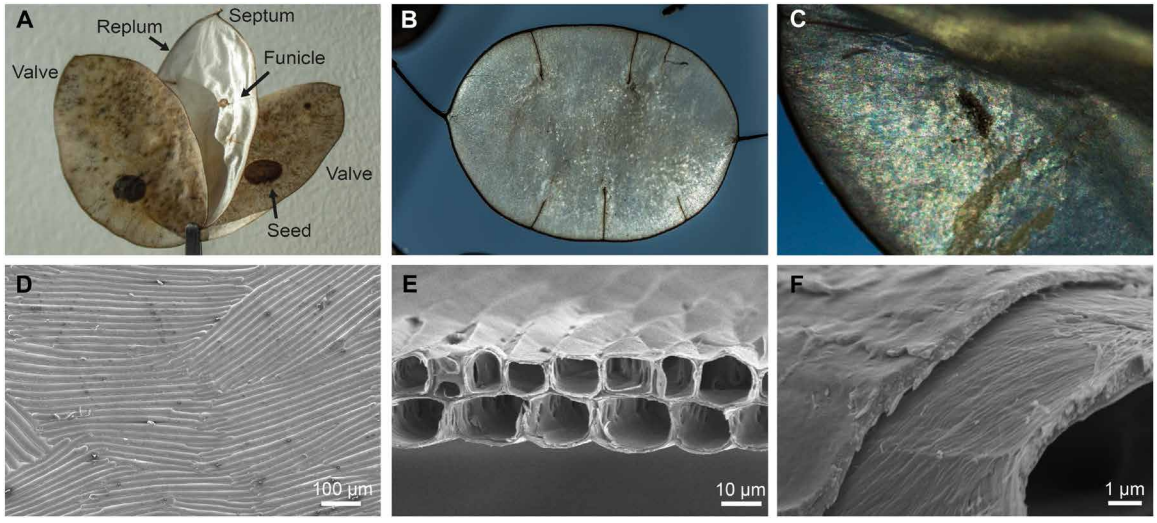

Fig. 1. *L. annua* seedpod macroscopic appearance and hierarchical morphology. (**A**) Macroscopic photographs of an *L. annua* seedpod showing the matte two external valves surrounding the internal silvery-white septum. The seeds attached to the valves developed from the septum's funicles. (**B**) Macroscopic photograph of the highly reflective septum with average size of ~3.1 × 4.6 cm and (**C**) closeup photograph of the septum showing thin-film interference colors and a texture reminiscent of arrays of colorful parallel elongated cells. (**D**) Top view SEM image of the septum showing multidomains made by 1D arrays of cylindrical cells oriented in parallel fashion inside each domain. (**E**) Cross-sectional SEM image of the septum hollow cell bilayer arrays. (**F**) High-magnification cross-sectional SEM image of an individual hollow cell with visible thin-film assembly in the cell wall cladding and alignment of the nanofibrils along the cell circumference. Photo credit: F.G.O., Tufts University.

electron microscopy (SEM) imaging of the surface of the *Lunaria* septum in top view displays multiple ordered domains with average size of few hundreds of square micrometers. Each domain consists of a one-dimensional (1D) array of elongated cells (Fig. 1D), which tend to arrange parallel to one another, especially in proximity to the septum edge. Cross-sectional analysis of the septum reveals the bilayer arrangement of the cells, which are reminiscent of hollow-core fibers with thin-film cellulose cladding in the cell wall (Fig. 1E and fig. S2). The two laminae of 1D hollow-core cell arrays are measured to have a combined average thickness of 18.6 ± 3.5 μm (N = 15). The cells in the arrays have cross-sectional shapes ranging between quasi-circular to near rectangular, possibly due to the natural variability in the development of the meristematic tissue in the septum (*28*). On average, the cells' eccentricity varies with inner widths of 12.3 ± 3.0 μm and heights of 9.6 ± 1.5 μm. The thin-film cladding in the cell wall is considerably thinner, measuring only 0.6 ± 0.3 μm, as measured by SEM cross sections (N = 15). The structural hierarchy of the construct is further revealed through analysis of the individual hollow-core cells that display cellulose nanofibrillar morphology that assembles in multiple thin films along the cell wall with individual thickness of few hundreds of nanometers, ultimately resulting in the hollow-core cell cladding (Fig. 1F). The hierarchical assembly of cellulose nanofibrils is visible in electron microscopy images, aligned along the cell circumference (fig. S3).

Structural color by thin-film interference

The characteristic length scales and morphology of the *L. annua* septum define its optical properties (Fig. 2). The thin cellulose cladding, present in the individual cell walls, produces coloration through thin-film interference (Fig. 2A). This coloration mechanism is also responsible for the coloration observed in insect wings (*36*, *37*) and mollusk shells (*35*), among others. The characteristic thickness of the individual layers in the cell wall is commensurate with the wavelength of visible light with values around 310 ± 120 nm (N = 26) and variability in layer thickness due to natural variation within the layer assembly and cell drying during fruit development. This variability in the cellulose thin-film cladding thickness along each cell (Fig. 2B) induces a broad range of reflected colors that span the entire visible range and display high reflectance with respect to a white diffuser standard (Fig. 2, B to I). Structural coloration is predominantly observed on the top surface of the cells and not at their boundaries due to the low numerical aperture of the used objective, which limits the angular collection of the reflected light (*4*). The colored regions along each elongated cell are individually resolved at the microscopic scale, as shown by optical microspectroscopy (collection spot Ø ~4 μm) (Fig. 2, A and B). The reflectance intensity modulation (Fig. 2B) is thought to originate from thin layers of cellulose in the cell cladding, as confirmed by finite-difference time-domain (FDTD) simulations of flat cellulose thin film in air (fig. S4) (*38*, *39*). Because of the limited size of the colored regions on the cell wall surface and their close proximity, the individual reflected colors cannot be macroscopically resolved, and, instead, they merge together to create a broadband response, which gives the *Lunaria* septum its typical silvery-white appearance (Fig. 1B). This process is known as additive color mixing principle, and it has been reported also for chitin-based structures in many butterfly wings (*40*–*42*). The *Lunaria* macroscopic silvery-white appearance is confirmed by the reflectance of white light incident on the top section of the cladding in the normal direction acquired over large areas (collection spot Ø ~60 μm). This shows a broadband reflectance signal ~40 to 50%, with respect to a white diffuser standard as measured by optical microspectroscopy, with increasing reflectance intensity observed at higher wavelengths (Fig. 2C).

To elucidate the spatial distribution of structural color in the septum (Fig. 2, A and D), we carried out spectral analysis as a function of fruit topography by bright-field multispectral microscopy. This technique allows the collection of 3D image stacks (x, y, and reflectance

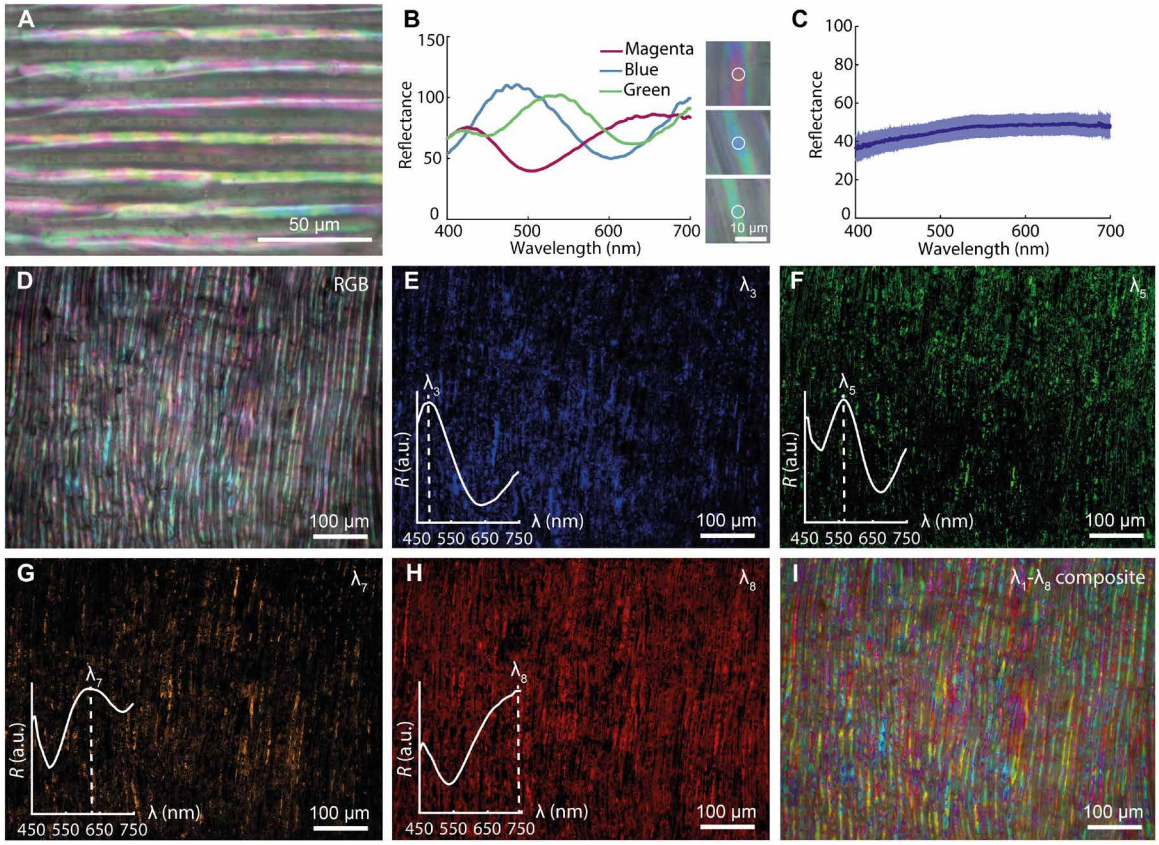

Fig. 2. Optical characterization of *L. annua* septum. (**A**) Bright-field reflection micrograph of the septum surface observed in top view showing thin-film interference–like colors spanning the entire visible spectrum. (**B**) Reflectance spectra collected within single-colored regions, reflecting magenta, blue, and green, and corresponding optical micrographs (white circle indicates the fiber collection spot, Ø ~4 μm, normalized to a white diffuser). (**C**) Average reflectance spectrum of the septa collected over large areas (collection spot Ø ~60 μm, normalized to a white diffuser) is indicated by the solid line and SD is the shaded areas. (**D** to **I**) Multispectral bright-field reflection analysis of the septum: The broadband reflectance RGB image (D) can be unmixed in individual false-color spectral maps, each defined by the wavelength λ_i, that identifies the spatial distribution of each selected spectral response corresponding to the spectral bands whose maximum reflectance peaks are, respectively, λ_3 ~485 nm (E), λ_5 ~564 nm (F), λ_7 ~621 nm (G), and λ_8 ~740 nm (H), as verified by the reflectance spectra shown in the insets. a.u., arbitrary units. (I) The individual spectral maps, defined by the wavelengths λ_1-λ_8, can be recombined to generate a false-color composite spectral map, which emphasizes the multicolored response of the septum.

intensity in a specific wavelength range λ_{start}-λ_{end} with a step size $\Delta\lambda$) that contain spectral information for every pixel of the image (*43*), thus allowing to have a spectrally resolved spatial map of the individual reflectance components from *Lunaria*'s single-colored regions (fig. S5A). The reflected light from the *Lunaria* septum was mapped in the λ = 450- to 750-nm range with a step size $\Delta\lambda$ = 3 nm through a tunable liquid crystal filter camera to illustrate the spatial distribution and variability of the thin-film cell wall cladding structures (Fig. 2, D to I). From the acquired red-green-blue (RGB) image (Fig. 2D), eight spectral components reflecting in different portions of the visible spectrum could be identified (fig. S5, B and C). The individual spectral responses of four representative spectral components were isolated and plotted (Fig. 2, E to H). These false-color multispectral images identify the specific spectral regions, along each *Lunaria* cell, where the cellulose thin films are more compact (spectral response λ_3 ~485 nm and λ_5 ~564 nm, respectively, blue and green regions; Fig. 2, E and F), and, conversely, where the films are thicker (spectral response λ_7 ~621 nm and λ_8 ~740 nm, respectively, orange and red regions; Fig. 2, G and H). Combining the individual spectral maps allows the generation of a composite image that better illustrates the distribution of spectral response of the *Lunaria* septum within each domain and along each cell (Fig. 2I).

Mechanical properties

In addition to its optical properties, the *L. annua* septum also exhibits remarkable mechanical properties that derive from the unique arrangement of a strong structural material (i.e., cellulose nanofibrils) (*44*) in arrays of hollow elongated cells, ultimately resulting in a membrane that is, at the same time, strong and flexible.

Within the two laminae that form the septum membrane, the 1D hollow-core cell array domains are observed to arrange parallel, perpendicular, and at an angle to one another, as shown by SEM cross sections (respectively Fig. 3, A to C). The domains with arrays perpendicular or at an angle account for the strength of the septum, whereas the domains with parallel arrays promote bending without crack formation (Fig. 3D). This regular arrangement of the cellulose cells in the arrays can also be confirmed by propagating light through the septum. The relative orientation of the cell arrays in the bilayer exhibits a diffracted far-field pattern that displays either a linear interference pattern (Fig. 3E, top) or intersecting diffraction lines (Fig. 3E,

bottom). The former confirms the presence of arrays with elongated cells with similar planar orientation in the two laminae, whereas the latter is indicative of cells oriented along different directions in the bilayer construct. Calculation of the grating pitch according to the diffraction equation yields a value of 18.3 ± 3.7 μm, in agreement with the pitch measured by SEM, which gives 14.0 ± 2.5 μm. Because of the heterogeneous orientation of the cell array domains in the *Lunaria* septa, a macroscopic diffraction effect is not visible by measuring the angle-resolved reflectance of the septa (Fig. 3F). Despite this, this measurement confirmed the silvery-white appearance of the septum, resulting from the combined spectral contributions of all the individual hollow-core cells: despite the higher intensity recordings at higher collection angles, the reflectance appears largely invariant with the wavelength, which is common for white materials.

The distinctly thin cellulose cladding combined with the high cell size results in a structure with high air fill fraction, which accounts for the septum lightness (with a measured average weight of 10 to 20 mg per septum) and for the high porosity value of 72.11 ± 1.30% (N = 4), as measured by mercury porosimetry (Fig. 3G and fig. S6). Mechanical measurements were performed on sections of the *Lunaria* septum to confirm its distinctive properties (N = 9). In this case, the pods were hydrated for consistency with previously reported characterization of cellulose-based materials (*45*, *46*). These measurements reveal Young modulus values of E = 0.7 ± 0.1 GPa and ultimate tensile strength of E =12.4 ± 6.8 MPa, with stress-strain curves (fig. S7) indicative of a strong material with elastic behavior. The results in these conditions suggest that the *Lunaria* septa exhibit less strength than a purely cellulose-based crystalline sheet, such as cellulose nanocrystal films, and thus, it is less prone to develop brittle fractures as confirmed by the measured high percentage elongation of $\Delta = \Delta L/L$ = 1.8 ± 0.9. Again, a measure of variability in the parameters is associated to the variability occurring within naturally grown materials. This variation, however, is quite limited for the ultimate tensile strength and for the percentage elongation as represented by the Kernel density plots (Fig. 3, H to J). Taking into account the notably high porosity of the *Lunaria* septum, the density-normalized mechanical properties are consistent with literature values for cellulose microfibril films (Table 1) (*46*). Nevertheless, the *Lunaria* modulus and tensile strength are lower than the average values reported for crystalline systems, such as cellulose nanocrystal films (*45*), due to the presence of amorphous

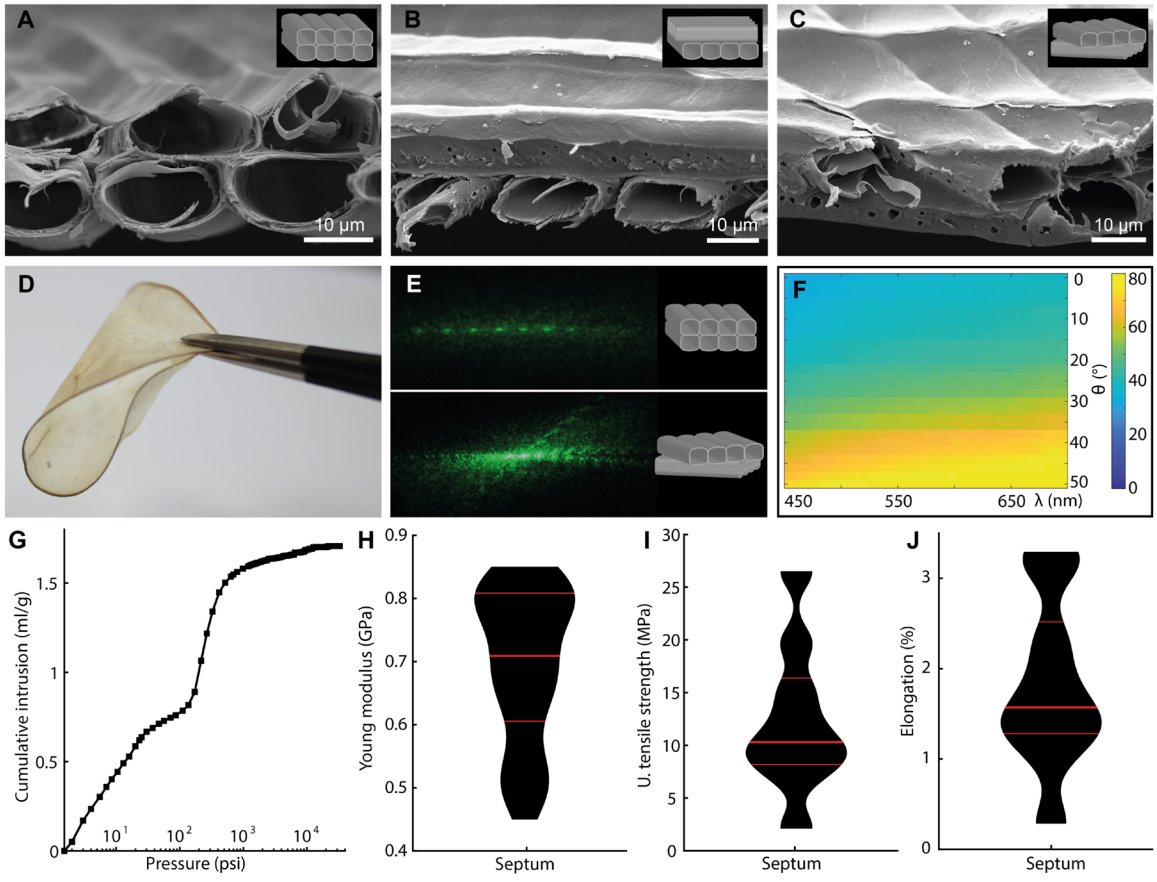

Fig. 3. Mechanical characterization of *L. annua* septum. SEM cross-sectional images and corresponding schematics (insets) of the observed cell array relative orientation in the septum: respectively, (**A**) parallel, (**B**) normal, and (**C**) at an angle. (**D**) Macroscopic picture of a bent *Lunaria* septum demonstrating high flexibility. (**E**) Transmission diffraction grating patterns with schematic representations of the layer relative orientation observed in cross section (insets). (**F**) The angular resolved reflectance of the septum, with intensity normalized against a Lambertian diffuser, demonstrates the overall reflectance capacity of the septum. (**G**) Representative weight-normalized cumulative volume of intruded mercury as a function of the applied pressure. Kernel density plots of (**H**) Young modulus, (**I**) ultimate tensile strength, and (**J**) elongation of the tested septa strips. The horizontal red lines divide the Kernel plots in the 25th (bottom), 50th (intermediate), and 75th percentile (top). Photo credit: G.G., Tufts University.

Table 1. Mechanical properties of *L. annua* in comparison with other cellulose-based films. Young modulus (E), ultimate tensile strength (σ), percentage elongation (ε), and corresponding density normalized values, respectively, (E/ρ), (σ/ρ), and (ε/ρ) for the *Lunaria* septa, cellulose microfibril films, and shear-aligned cellulose nanocrystal films. The minimum and maximum values are reported for the *L. annua* and cellulose microfibril films (*46*), whereas the values in axial and perpendicular direction to the cellulose nanocrystal alignment are reported for the cellulose nanocrystal films (*45*). The density-normalized values are calculated assuming a density of 0.26, 1.5, and 1.55 g/cm^3 for the *Lunaria* septa, the cellulose microfibril films, and the cellulose nanocrystal films, respectively.

	E (GPa)	E/ρ (GPa)/(g cm^{-3})	σ (MPa)	σ/ρ (MPa)/(g cm^{-3})	ε (%)	ε/ρ (%)/(g cm^{-3})
Lunaria septa	0.5 to 0.8	1.9 to 3.2	2.2 to 26.4	8.4 to 103	0.3 to 3.3	1 to 12.7
Cellulose microfibril films (*46*)	1 to 17.5	0.7 to 11.7	30 to 155	20 to 103.3	2.5 to 11.5	1.7 to 7.7
Cellulose nanocrystal films (*45*)	6.7 to 29.7	4.3 to 19.2	48 to 77	31 to 49.6	0.3 to 0.9	0.2 to 0.6

regions along the nanofibrils and to the variation of the array orientations in the septa.

DISCUSSION

The *Lunaria* septum is a notable example of naturally occurring cellulose assembly into an end material with distinctive optical and mechanical properties. In contrast with most examples of structurally colored fruits reported thus far, the *L. annua* fruit grows in temperate regions and in planar format, displaying silvery-white structural color on an internal membrane, the septum. This is quite unusual as, commonly, structural color in fruits is located in the epicarp, whose external location is thought to be functional for signaling with animals for seed dispersal. The cellulose fibril assembly in the hollow-core cells induces thin-film interference–like colors due to the presence of thin cellulose layers in the cell wall. These are responsible for the broad range of thin-film interference–like colors observed microscopically and, because of the limited size of each single-colored region, produce macroscopically a reflected silvery-white coloration due to the additive color mixing principle. The silvery appearance of the white coloration is especially visible at high observation angles, and it is thought to arise from high regularity of the cellulose thin films in the cells forming the septum, which show only minimal defects. The presence of a higher amount of defects would, instead, generate a more angular independent chalky-white appearance due to the predominance of the scattered light over the reflected light (*47*). The elongated cell parallel arrangement within the microdomains is responsible for the local diffraction effect. The hollow cell multidomain network assembles into an ultralight membrane with high porosity, which accounts for the lightness of the construct and for high flexibility of the septum. In summary, the *L. annua* fruit, besides being optically selective, is mechanically strong and tough, embodying the coexistence of structural hierarchy and physical function, which can serve as inspiration for advanced classes of bioinspired, robust, light, and spectrally selective devices. The *L. annua* fruit incorporates the uniquely distinctive, multifunctional, and hierarchical properties that make naturally occurring materials inspiring templates for high-performance technological materials.

MATERIALS AND METHODS

Materials

Dry seedpods of *L. annua* were collected in Italy in fall 2017–2018. The septa of the seedpods were kept in a dry and cool place and used without further treatment unless otherwise specified. *L. annua* septa average size and weight were calculated from 22 individual septa, and the SD was used as error bars.

Plant photographs

Digital images of the *L. annua* dry seedpods were taken with a DSLR (digital single-lens reflex) camera (Canon Rebel EOS-SL1). The RAW image files were adjusted for exposure and contrast.

Optical microscopy and spectroscopy

A customized Olympus Inverted IX71 microscope equipped with a charge-coupled device camera (Thorlabs, DCC1645C) and with a halogen lamp (Olympus, U-LH100L-3) as light source was used to perform optical microscopy. Bright-field reflection images were collected using 10× [Olympus, UPlanFL N, numerical aperture (NA) 0.3], 20× (Olympus, LUCPlanFL N, NA 0.45), and 50× (Olympus LMPlanFL N, NA 0.5) objectives. To quantify the reflectance of the *L. annua* septa, the microscope was connected to a spectrometer (Ocean Optics, USB2000) through an optical fiber (Ocean Optics, P200-2-UV-VIS, 200-μm core size, and P600-2-UV-VIS, 600-μm core size) mounted in confocal configuration. The reflectance spectra were normalized against a white Lambertian diffuser [reflectivity >99% (400 to 1500 nm); Labsphere], smoothed and plotted using the software MATLAB R2018b. To perform multispectral analysis, the microscope was coupled to a multispectral camera (CRI Nuance EX). The septa were observed using a 20× objective (Olympus, UPlanFL N, NA 0.3) in bright-field reflection, and the spectral maps were acquired in the range 450 to 750 nm with a step size of 3 nm. The software Nuance 3.0.2 was used to acquire and unmix the maps in different spectral components. The eight selected reflectance peak wavelengths and the corresponding false colors used for the spectral maps were as follows: λ_1 ~489 and ~738 nm, purple; λ_2 ~477 and ~684 nm, magenta; λ_3 ~485 nm, blue; λ_4 ~525 nm, cyan; λ_5 ~564 nm, green; λ_6 ~579 nm, yellow; λ_7 ~621 nm, orange; and λ_8 ~740 nm, red.

Angular-resolved optical spectroscopy

The scattering behavior of the *L. annua* septum was measured using a bespoke goniometer equipped with a lamp (MI 150 fiber illuminator, Edmund Optics) and a spectrometer (USB2000, Ocean Optics). The sample was mounted on a fixed stage and illuminated by a 400-μm core fiber (R400-7-VIS-NIR, Ocean Optics) coupled to the lamp at −30° incident angle with respect to the normal to the sample (light spot size Ø ~10 mm). The scattered light was collected by a 200-μm core fiber (Ocean Optics) coupled into the spectrometer and mounted

on a manual rotating stage. The recorded light intensity was normalized with respect to a white Lambertian diffuser [reflectivity >99% (400 to 1500 nm); Labsphere].

Diffraction grating patterns

The *L. annua* septa were illuminated by a green laser (λ = 534.5 nm; Melles Griot) positioned normally with respect to the fruit's septum. The transmission diffraction patterns were collected on a screen positioned 15 cm away from the samples and captured using a camera (Canon Rebel EOS T1i) located at the back of the screen. The software ImageJ was used to analyze the patterns.

Optical modeling

The software Lumerical FDTD Solutions (Lumerical Inc.) was used to simulate the light interaction with the *L. annua* septa, by using a FDTD method. To account for the objective focus depth ($d < 4.5$ μm), only the outer portion of a single cellulose hollow cell lamina was modeled. This was simplified to a 1D flat thin cellulose film (*38*) ($n_{cellulose} = 1.5808$) surrounded by air ($n_{air} = 1$). To simulate the reflectance of regions with magenta, blue, and green appearance, the cellulose layer thickness (t) was set to $t_{magenta} = 318$ nm, $t_{blue} = 380$ nm, and $t_{green} = 418$ nm. These values were in agreement with the cellulose layer thickness measured from SEM cross sections of *L. annua* septa. A plane wave (λ = 400 to 800 nm) incident normal to the thin film was used as light source and a frequency-domain field and power monitor, positioned behind the light source, collected the reflected light. The boundary conditions were set to periodic and absorbing (perfectly matching layer), respectively, for the direction normal and parallel to the light source propagation.

Electron microscopy

The *Lunaria* septa were cryofractured by immersing them in liquid nitrogen for 3 min and subsequently crushing them. The fragments were mounted on aluminum stubs by using carbon tape. To ensure electrical conductivity, the stubs were sputtered with ~10 nm of gold using an Emitech SC7620 sputter coater. The top view and the cross sections of the septa were imaged using a Zeiss EVO MA10 SEM with a secondary electron detector at 8 to 10 kV and 4 to 6 mm as the working distance. The SEM images were analyzed with the software ImageJ to determine the septa characteristic sizes. At least 15 measurements were acquired for each set, and the reported values were the average values with errors bars given by the SD.

X-ray diffraction

The XRD spectrum of the *Lunaria* septa was acquired using a PANalytical X'Pert Pro XRPD (x-ray powder diffraction) x-ray diffractometer operating with a Cu Kα radiation source (1.5418 Å) and recorded in the 2θ range of 5° to 40° for 30 min at 45 kV and 40 mA at room temperature. The XRD raw spectrum was smoothed and normalized using the software MATLAB R2018b. The XRD measurements were performed at the Center for Material Science and Engineering at Massachusetts Institute of Technology.

Tensile measurements

The tensile measurements of the *Lunaria* septa were carried out on an Instron 3366 tensile testing system. Rectangular strips (35 mm × 3 mm) were cut from the septa (conditioned at 50% relative humidity and 21°C for 6 days), paying attention to avoid the funicles and any region close to edge. The individual strips were directly mounted on the grips of the instrument in tensile configuration with a nominal cell load of 100 N. The gauge length was quantified before the measurement for each individual strip (14 to 20 mm), and an average thickness value of 20 μm was used, as inferred from the SEM imaging. The strips were preloaded up to 0.02 N with a pulling velocity of 0.05 mm/s, while during the test, they were pulled at 0.5 mm/s. The ultimate tensile strength, the Young modulus, and the percentage elongation were calculated from the stress-strain curve. The Kernel density plots were calculated using the software MATLAB R2018b and truncating the distributions at the minimum and maximum values for each plot.

Porosimetry

To measure the porosity of the *Lunaria* septa, mercury porosimetry was performed using an AutoPore IV porosimeter (Micromeritics, GA) with a pressure range of 0 to 33,000 psi. From the raw data of intruded volume versus pressure, differential intrusion as a function of pore size was calculated using the Washburn equation (assuming contact angle θ = 130° and surface tension γ = 0.485 N/m). To ensure enough material in the penetrometer, three septa were used for each porosity measurement. In total, four measurements were performed for statistical reliability and repeatability of the porosity measurement.

SUPPLEMENTARY MATERIALS

Supplementary material for this article is available at http://advances.sciencemag.org/cgi/content/full/6/27/eaba8966/DC1

View/request a protocol for this paper from *Bio-protocol*.

REFERENCES AND NOTES

1. S. Kinoshita, *Structural Colors in the Realm of Nature* (World Scientific Publishing Co, 2010); https://www.worldscientific.com/worldscibooks/10.1142/6496.
2. V. E. Johansen, O. D. Onelli, L. M. Steiner, S. Vignolini, *Photonics in Nature: From Order to Disorder* (Springer, Cham, 2017), pp. 53–89.
3. S. Vignolini, E. Moyroud, B. J. Glover, U. Steiner, Analysing photonic structures in plants. *J. R. Soc. Interface* **10**, 20130394 (2013).
4. S. Vignolini, P. J. Rudall, A. V. Rowland, A. Reed, E. Moyroud, R. B. Faden, J. J. Baumberg, B. J. Glover, U. Steiner, Pointillist structural color in *Pollia* fruit. *Proc. Natl. Acad. Sci. U.S.A.* **109**, 15712–15715 (2012).
5. S. Vignolini, T. Gregory, M. Kolle, A. Lethbridge, E. Moyroud, U. Steiner, B. J. Glover, P. Vukusic, P. J. Rudall, Structural colour from helicoidal cell-wall architecture in fruits of *Margaritaria nobilis*. *J. R. Soc. Interface* **13**, 20160645 (2016).
6. H. M. Whitney, M. Kolle, P. Andrew, L. Chittka, U. Steiner, B. J. Glover, Floral iridescence, produced by diffractive optics, acts as a cue for animal pollinators. *Science* **323**, 130–133 (2009).
7. E. Moyroud, T. Wenzel, R. Middleton, P. J. Rudall, H. Banks, A. Reed, G. Mellers, P. Killoran, M. M. Westwood, U. Steiner, S. Vignolini, B. J. Glover, Disorder in convergent floral nanostructures enhances signalling to bees. *Nature* **550**, 469–474 (2017).
8. M. Jacobs, M. Lopez-Garcia, O.-P. Phrathep, T. Lawson, R. Oulton, H. M. Whitney, Photonic multilayer structure of *Begonia* chloroplasts enhances photosynthetic efficiency. *Nat. Plants.* **2**, 16162 (2016).
9. L. M. Steiner, Y. Ogawa, V. E. Johansen, C. R. Lundquist, H. Whitney, S. Vignolini, Structural colours in the frond of *Microsorum thailandicum*. *Interface Focus.* **9**, 20180055 (2018).
10. K. R. Thomas, M. Kolle, H. M. Whitney, B. J. Glover, U. Steiner, Function of blue iridescence in tropical understorey plants. *J. R. Soc. Interface* **7**, 1699–1707 (2010).
11. S. Vignolini, E. Moyroud, T. Hingant, H. Banks, P. J. Rudall, U. Steiner, B. J. Glover, The flower of *Hibiscus trionum* is both visibly and measurably iridescent. *New Phytol.* **205**, 97–101 (2015).
12. S. Vignolini, M. P. Davey, R. M. Bateman, P. J. Rudall, E. Moyroud, J. Tratt, S. Malmgren, U. Steiner, B. J. Glover, The mirror crack'd: Both pigment and structure contribute to the glossy blue appearance of the mirror orchid, *Ophrys speculum*. *New Phytol.* **196**, 1038–1047 (2012).
13. D. W. Lee, Ultrastructural basis and function of iridescent blue colour of fruits in *Elaeocarpus*. *Nature* **349**, 260–262 (1991).
14. D. W. Lee, G. T. Taylor, A. K. Irvine, Structural fruit coloration in *Delarbrea michieana* (Araliaceae). *Int. J. Plant Sci.* **161**, 297–300 (2000).

15. J. P. Vigneron, M. Rassart, Z. Vértesy, K. Kertész, M. Sarrazin, L. P. Biró, D. Ertz, V. Lousse, Optical structure and function of the white filamentary hair covering the edelweiss bracts. *Phys. Rev. E Stat. Nonlin. Soft Matter Phys.* **71**, 011906 (2005).
16. M. Lopez-Garcia, N. Masters, H. E. O'Brien, J. Lennon, G. Atkinson, M. J. Cryan, R. Oulton, H. M. Whitney, Light-induced dynamic structural color by intracellular 3D photonic crystals in brown algae. *Sci. Adv.* **4**, eaan8917 (2018).
17. C. Hebant, D. W. Lee, Ultrastructural basis and developmental control of blue iridescence in *Selaginella* leaves. *Am. J. Bot.* **71**, 216–219 (1984).
18. M. Kolle, A. Lethbridge, M. Kreysing, J. J. Baumberg, J. Aizenberg, P. Vukusic, Bio-inspired band-gap tunable elastic optical multilayer fibers. *Adv. Mater.* **25**, 2239–2245 (2013).
19. K. L. Willdenow, C. F. Schwägrichen, C. von Linné, H. F. Link, *Species Plantarum: Exhibentes Plantas Rite Cognitas, Ad Genera Relatas, Cum Differentiis Specificis, Nominibus Trivialibus, Synonymis Selectis, Locis Natalibus, Secundum Systema Sexuale Digestas* (Impensis Laurentii Salvii, Holmiae: 2011); http://www.biodiversitylibrary.org/bibliography/669.
20. M. A. Beilstein, I. A. Al-Shehbaz, E. A. Kellogg, Brassicaceae phylogeny and trichome evolution. *Am. J. Bot.* **93**, 607–619 (2006).
21. GBIF, *Lunaria* annua L. Global Biodiversity Information Facility; https://www.gbif.org/species/5373324.
22. I. A. Al-Shehbaz, *Brassicaceae (Mustard Family)* (eLS, John Wiley & Sons, Ltd: Chichester, 2011).
23. Ł. Łangowski, N. Stacey, L. Østergaard, Diversification of fruit shape in the Brassicaceae family. *Plant Reprod.* **29**, 149–163 (2016).
24. P. Leins, C. Erbar, *Flower and Fruit : Morphology, Ontogeny, Phylogeny, Function and Ecology* (Schweizerbart, 2010).
25. M. E. Fournier, On the constitution of the fruit in the Cruciferae. *Ann. Mag. Nat. Hist.* **16**, 299–301 (1865).
26. C. Leins, K. Fligge, C. Erbar, Silique valves as sails in anemochory of *Lunaria*(Brassicaceae). *Plant Biol.* **20**, 238–243 (2018).
27. G. B. Seymour, L. Østergaard, N. H. Chapman, S. Knapp, C. Martin, Fruit development and ripening. *Annu. Rev. Plant Biol.* **64**, 219–241 (2013).
28. J. Spence, Y. Vercher, P. Gates, N. Harris, 'Pod shatter' in *Arabidopsis thaliana Brassica napus* and *B. juncea*. *J. Microsc.* **181**, 195–203 (2003).
29. S. Mosti, C. Ross Friedman, F. Piccolin, P. Di Falco, A. Papini, The unusual tegumental tissues of the *Lunaria annua* (Brassicaceae) seed: A developmental study using light and electron microscopy. *Flora Morphol. Distrib. Funct. Ecol. Plants.* **207**, 828–837 (2012).
30. F. Bouman, Integument initiation and testa development in some *Cruciferae*. *Bot. J. Linn. Soc.* **70**, 213–229 (1975).
31. Y. Guo, E. Mietkiewska, T. Francis, V. Katavic, J. M. Brost, M. Giblin, D. L. Barton, D. C. Taylor, Increase in nervonic acid content in transformed yeast and transgenic plants by introduction of a *Lunaria annua* L. 3-*ketoacyl-CoA synthase* (*KCS*) gene. *Plant Mol. Biol.* **69**, 565–575 (2009).
32. S. Sagner, Z.-W. Shen, B. Deus-Neumann, M. H. Zenk, The biosynthesis of lunarine in seeds of *Lunaria annua*. *Phytochemistry* **47**, 375–387 (1998).
33. G. S. Dodos, D. Karonis, F. Zannikos, E. Lois, Renewable fuels and lubricants from *Lunaria annua* L. *Ind. Crop Prod.* **75**, 43–50 (2015).
34. R. H. Atalla, D. L. Vanderhart, Native cellulose : A composite of two distinct crystalline forms. *Science* **223**, 283–285 (1984).
35. A. H. Pfund, The colors of mother-of-pearl. *J. Franklin Inst.* **183**, 453–464 (1917).
36. C. Kilchoer, U. Steiner, B. D. Wilts, Thin-film structural coloration from simple fused scales in moths. *Interface Focus.* **9**, 20180044 (2019).
37. E. Shevtsova, C. Hansson, D. H. Janzen, J. Kjærandsen, Stable structural color patterns displayed on transparent insect wings. *Proc. Natl. Acad. Sci. U.S.A.* **108**, 668–673 (2011).
38. P. H. Hermans, *Contribution to the Physics of Cellulose Fibres: A Study of Sorption, Density, Refractive Power and Orientation* (Elsevier Publishing Company Inc., Amsterdam, The Netherlands, 1946).
39. K. S. Yee, Numerical solution of initial boundary value problems involving maxwell's equations in isotropic media. *IEEE Trans. Antennas Propag.* **14**, 302–307 (2004).
40. P. Vukusic, R. Kelly, I. Hooper, A biological sub-micron thickness optical broadband reflector characterized using both light and microwaves. *J. R. Soc. Interface* **6**, S193–S201 (2009).
41. B. D. Wilts, P. Pirih, K. Arikawa, D. G. Stavenga, Shiny wing scales cause spec(tac)ular camouflage of the angled sunbeam butterfly, *Curetis acuta*. *Biol. J. Linn. Soc.* **109**, 279–289 (2013).
42. M. A. Giraldo, *Butterfly Wing Scales : Pigmentation and Structural Properties* (2008); https://www.rug.nl/research/portal/files/14499068/thesis.pdf.
43. R. Levenson, J. Beechem, G. Mcnamara, Spectral imaging in preclinical research and clinical pathology. *Anal. Cell. Pathol.* **35**, 339–361 (2012).
44. Y. Nishiyama, Structure and properties of the cellulose microfibril. *J. Wood Sci.* **55**, 241–249 (2009).
45. A. B. Reising, R. J. Moon, J. P. Youngblood, Effect of particle alignment on mechanical properties of neat cellulose nanocrystal films. *J-FOR.* **2**, 32–41 (2012).
46. R. J. Moon, A. Martini, J. Nairn, J. Simonsen, J. Youngblood, Cellulose nanomaterials review: Structure, properties and nanocomposites. *Chem. Soc. Rev.* **40**, 3941–3994 (2011).
47. D. L. Fox, *Animal Biochromes and Structural Colours: Physical, Chemical, Distributional & Physiological Features of Coloured Bodies In The Animal World* (University of California Press, 1976).

Acknowledgments: G.G. would like to thank G. Matzeu for the discussion on the tensile measurement setup. **Funding:** F.G.O. acknowledges support from the Office of Naval Research (ONR award N00014-13-1-0596 and N00014-19-1-2399), and B.M. acknowledges support from the Office of Naval Research (ONR award N00014-18-12258) and the National Science Foundation (NSF award CMMI-1752172). **Author contributions:** G.G. and F.G.O. designed the research work. G.G. performed the optical, morphological, and mechanical measurements. H.S. and B.M. performed the porosimetry measurements. G.G., H.S., B.M., and F.G.O. analyzed the data. G.G. and F.G.O. cowrote the paper. All the authors discussed the results and commented on the paper. **Competing interests:** The authors declare that they have no competing interests. **Data and materials availability:** All data needed to evaluate the conclusions in the paper are present in the paper and/or the Supplementary Materials. Additional data related to this paper may be requested from the authors.

Submitted 14 January 2020
Accepted 22 May 2020
Published 1 July 2020
10.1126/sciadv.aba8966

Citation: G. Guidetti, H. Sun, B. Marelli, F. G. Omenetto, Photonic paper: Multiscale assembly of reflective cellulose sheets in *Lunaria annua*. *Sci. Adv.* **6**, eaba8966 (2020).